A new mechanism for brittle failure in garnets

Renelle Dubosq[1], David A. Schneider[2], Alfredo Camacho[3], Baptiste Gault[1,4]
[1]*Max-Planck-Institüt für Eisenforschung GmbH, Germany*
[2]*Department of Earth and Environmental Sciences, University of Ottawa, Canada*
[3]*Department of Earth Sciences, University of Manitoba, Canada*
[4]*Department of Materials, Royal School of Mines, Imperial College London, UK*

Corresponding author: Renelle Dubosq (renelle.dubosq@gmail.com)
† t: +49 176 7758 3379
Max-Planck-Straße 1
40237 Düsseldorf, Germany
https://orcid.org/0000-0002-1364-1574

David A. Schneider
150 Louis Pasteur Pvt
Ottawa, ON, Canada
K1N 6N5
https://orcid.org/0000-0002-9665-4927

Alfredo Camacho
125 Dysart Road
Winnipeg, MB, Canada
R3T 2N2
https://orcid.org/0000-0002-8517-168X

Baptiste Gault
Max-Planck-Straße 1
40237 Düsseldorf, Germany
And
Exhibition Road
London, SW7 2AZ, UK
https://orcid.org/0000-0002-4934-0458

Highlights

- High-spatial resolution microscopy is used to study garnet deformation mechanisms
- Atom probe tomography reveals Fe-rich nanoclusters at high-angle grain boundaries
- Fe-rich nanoclusters lead to strain hardening and mechanical failure in garnet

Abstract

Garnet is a high-strength mineral and preserves structures that can consequently be used to understand the flow strength and evolution of stress within the lower crust. Yet, the deformation mechanisms at the brittle-ductile transition of garnet remain ambiguous. Here, we study garnet porphyroclasts from an eclogite facies mylonite (central Australia) to investigate the mechanisms by which garnet is deformed under relatively dry, lower crustal conditions. Electron backscatter diffraction analysis reveals bands of small, relatively strain-free garnet with scattered orientations, outlined by polygonal to lobate high-angle grain boundaries cross-cutting the garnet porphyroclasts. Atom probe tomography of a high-angle grain boundary shows Fe enrichment in the form of planar and equally spaced arrays of Fe-rich nanoclusters. Our experiments demonstrate Fe segregation along grain boundaries of garnet, resulting in the nucleation of Fe-rich nanoclusters that can act as barriers for migrating dislocations which leads to strain-hardening that facilitates mechanical failure. The occurrence of strain-hardening in garnet potentially contributes to crustal strengthening that can lead to seismicity at depths.

Keywords

garnet, atom probe tomography, strain-hardening, nanostructures, crystal-plasticity

1. Introduction

The mechanical behaviour of the lithosphere and the variation of strength with depth has been an enduring topic in tectonics. It is generally accepted that the yield strength of the lithosphere at geological timescales can be simplified using the "Christmas tree" envelope model (Goetze and Evans, 1979). In this model, the lithosphere is assumed to be a single uniform layer with an upper brittle part that follows a law of static friction (i.e., Byerlee’s law) and a lower ductile part that follows a viscous flow law (Byerlee, 1978; Wang, 2021). In truth, the lithosphere consists of multiple layers where brittle and ductile behaviour alternate (e.g., Bürgmann and Dresen, 2008; Kohlstedt et al., 1995; Ellis and Wang, 2022). Other more sophisticated forms of the strength profile for the continental lithosphere have been proposed including the well-known "jelly sandwich" and "crème brûlée" models (Burov and Watts, 2006; Jackson, 2002). Such models are essential for geodynamic modelling and reconstructing the evolution and stabilization of continents (e.g., Audet and Bürgmann, 2011). Most of these models, however, assume a brittle upper layer and a ductile middle to lower layer separated by a steady-state transition zone. Consequently, the lower continental crust is thought to be too hot to deform by brittle fracturing, and frictional sliding at great depth is commonly considered to be a paradox (Green and Houston, 1995; White, 2012). Despite these assumptions, seismicity indicators such as pseudotachylytes in deeply exhumed rocks demonstrate earthquakes do occur at depths (>50 km; e.g., Austrheim and Boundy, 1994). Since the macroscopic rheology of the lower crust is governed by the microscopic mechanical behaviour of its component minerals, microstructures within these minerals are often used to infer its mechanical behaviour (e.g., Kavner et al., 2007; Mainprice et al., 2004; Phillips and Ji, 2021). Under lower crustal conditions, most rock-forming minerals such as quartz and feldspars deform by ductile creep, which can obscure microstructures associated with seismic events (Kirkpatrick and Rowe, 2013). Garnet, notably, is considered mechanically and chemically stable under elevated temperatures and commonly preserves microstructures related to seismicity (e.g., Mancktelow et al., 2022; Trepmann and Stöckhert, 2002). Although garnet is not the most predominant mineral in the lower crust, it becomes increasingly important with depth constituting a large modal proportion in metamorphosed rocks (up to 50%; Villaseca et al., 1999) and is assumed to play a significant role in crustal strengthening (e.g., Ingrin and Madon, 1995; Jin et al., 2001; Ji et al., 2003). Therefore, understanding the style and nature of garnet deformation under natural conditions is important for characterizing the flow strength and the stress history of the lower crust (Mainprice et al., 2004).

Although regarded as a high-strength mineral, the pressure-temperature conditions in the lower crust often exceed the conditions necessary for the onset of crystal-plastic behavior in garnet. Experimental deformation studies have showed that under typical strain rates for actively deforming regions (10^{-12}–10^{-15} s^{-1}; Behr and Platt, 2011), the onset for crystal-plasticity in garnet occurs at differential stresses of a few gigapascals and temperatures of 640–750°C (Karato et al., 1995; Wang and Ji, 1999). Some studies have consequently attempted to link the brittle behaviour of garnet at elevated temperatures to transient high fluid or melt pressures and fluid-assisted eclogitization of granulites (Austrheim and Boundy, 1994; Hacker et al., 2003; Rempel et al., 2006). Fracturing in garnet adjacent to pseudotachylites in deep-seated rocks has also been interpreted to be related to thermal shock due to frictional heating (Papa et al., 2018). Under dry, lower crustal conditions, fracturing may be related to transient high differential stresses from seismic rupture (Giuntoli et al., 2018; Hawemann et al., 2018, 2019a). Despite these efforts, the mechanisms of brittle fracture in garnet at elevated temperatures remain equivocal.

To determine the specific mechanisms by which garnet may be weakened under relatively dry, lower crustal conditions, we applied correlated microscopy using 2D and 3D structural and geochemical investigation at the near-atomic scale on a sample from a high-strain zone that formed within the base of the crust (35-40 km depths) of the Proterozoic Musgrave Province, central Australia (Gray, 1978; Camacho and Fanning, 1995). The well constrained pressure, temperature, and time history of the Musgrave Province make it an excellent field location to investigate the deformation mechanisms at the brittle-ductile transition for garnet (Gray, 1978; Camacho and Fanning, 1995; Camacho et al. 1997). We document enhanced diffusion of Fe along grain boundaries of recrystallized garnet, which apparently led to the nucleation of Fe-rich nanoclusters that may have acted as barriers for migrating dislocations. Once these barriers were established, the garnet underwent localized hardening and mechanical failure. Our data thus unequivocally establish the brittle behaviour of garnet during deformation in the lower crust.

2. Materials and Methods

2.1 Geological setting and sample description

The Musgrave Province is a Mesoproterozoic–Neoproterozoic granulite to amphibolite facies terrain located in central Australia that was formed by the amalgamation of different cratonic blocks during the Musgravian Orogeny (ca. 1120–1200 Ma; **Figure 1**; Gray, 1978; Camacho and Fanning, 1995). Granulite facies metamorphism at this time produced garnet-bearing quartzofeldapathic gneisses of peraluminous and intermediate composition (Camacho et al., 1997). The region was later heterogeneously overprinted during the Petermann Orogeny (ca. 550 Ma), by crustal-scale faults and high-strain shear zones including the Woodroffe Thrust, the Mann Fault, and the Davenport Shear Zone (DSZ; **Figure 1**; Collerson et al., 1972; Major, 1973; Camacho and

Fanning, 1995; Hawemann et al., 2018, 2019b; Wex et al., 2019). The eclogite facies DSZ is a W–E-striking strike-slip shear zone, with a near horizontal stretching lineation and strongly localized deformation (Camacho et al., 1997; Hawemann et al., 2019b). Peak conditions for the eclogite facies deformation were estimated at ~650°C and ~1.2 GPa (Ellis and Maboko, 1992; Camacho et al., 1997) under relatively dry conditions (<0.002 wt% H_2O; Wex et al. 2019). The sample studied herein is a quartzofeldspathic mylonite from the DSZ with relict granulite facies garnet porphyroclasts (**Figure 1, 2**). Within the sample, granulite facies garnet occurs as bands of millimetre-scale porphyroclasts (0.5–3.0 mm) that are parallel to the main planar foliation and as smaller (5–40 µm) neocrystallized eclogite facies porphyroblasts around relict garnets (**Figure 2a, b**; Camacho et al., 1997). Garnet porphyroclasts are strongly fractured, which occur as regularly spaced structures that are nearly perpendicular to the main foliation (**Figure 2a–c)**. These fractures do not propagate into the host rock matrix. Retrograde biotite (<5%) occurs between garnet clasts and within fractures (**Figure 2a–c**). Quartz occurs either as fine grains (<50 µm) with serrated boundaries (**Figure S1a**) or slightly larger elongated grains (up to 100 × 200 µm) exhibiting undulose extinction, deformation bands, and new subgrains forming around the edges (**Figure S1a**). Quartz also occurs as ribbons, defining the foliation (30 × 100 µm), with undulose extinction and polygonal subgrain development (**Figure S1b**). Comparatively, feldspar occurs as medium to coarse (0.2–0.5 mm × 0.5–2.5 mm) elongated lenticular porphyroclasts (**Figure S1c-d**). Feldspar porphyroclasts are oriented parallel to the main foliation and exhibit undulose extinction, folded and tapered twinning, and new subgrain development around the edges (**Figure S1c-d**).

2.2 2D microscopy

Primary characterization of the garnet porphyroclasts was performed by combining electron backscatter diffraction (EBSD) mapping and high-contrast backscattered electron (BSE) imaging to obtain quantitative and qualitative information of the crystalline structure and deformation state of the sample. All crystallographic data were collected at the Max-Planck-Institut für Eisenforschung GmbH (Düsseldorf, Germany) using a high-resolution field emission SEM Sigma (Carl Zeiss Microscopy, Germany) equipped with a Hikari (EDAX, USA) EBSD detector. Prior to analysis, the thin section was chemo-mechanically polished with an alkaline colloidal silica suspension and carbon-coated to establish conductivity. EBSD mapping was conducted first with analytical conditions set to an accelerating voltage of 15 kV and probe currents of 7.4 nA. The sample was tilted to 70° and brought to a working distance of 17.4 mm. Mapping was performed by using a hexagonal grid and a step size of 1.5 µm; the camera was operated by applying a 4×4 binning. The EBSD data was cleaned using the OIM Data Collection and Analysis software by combining the neighbour orientation correlation (clean-up level: 3) and confidence index standardization (CI: 0.1) functions. Misorientation deviation angle (misorientation of each pixel relative to grain average) and grain boundary maps were then created using the OIM software. Based on the EBSD data, highly-strained garnet porphyroclasts were selected for further analysis and are the main subject of this study.

High-contrast BSE imaging was subsequently conducted to further investigate the targeted microstructures. This imaging was performed on the Zeiss SEM Merlin (Carl Zeiss Microscopy, Germany) instrument at the Max-Planck-Institut für Eisenforschung GmbH. Analytical conditions for imaging were set to a 30 kV accelerating voltage, a 2.0 nA probe current and a working distance of 6.5 mm, allowing for the direct observation of crystal defects.

Energy-dispersive X-ray spectroscopy (EDX) was also performed on targeted grain boundaries on the Zeiss SEM Sigma using analytical conditions of 15 kV, probe currents of 7.4 nA, and a working distance of ~7.8 mm. EDX maps were collected by setting the counting time to 100 s and capturing 128-256 frames. Acquired EDX maps were subsequently processed using the EDAX APEX Data Collection and Analysis software.

An electron microprobe (EMP) was used to chemically characterize the garnet porphyroclasts. Qualitative X-ray mapping was performed using the Cameca SX-100 at the University of Manitoba (Canada). Mapping for Fe Kα, Mg Kα, Mn Kα, and Ca Kα were done at a 20 kV accelerating voltage, a 50 nA beam current, 1 μm beam size and 50 ms dwell time.

2.3 Atom probe tomography

A specimen was prepared from a high-angle grain boundary within the garnet by in situ lift-out (Thompson et al., 2007) for atom probe tomography (APT) in an attempt to investigate the detailed composition of some of the microstructural features at the near-atomic scale. The needle-shaped specimen was sharpened by annular milling at 30 kV on a dual-beam scanning electron microscope/focused ion beam FEI Helios Nanolab 600i at the Max-Planck-Institut für Eisenforschung GmbH and subsequently cleaned using the Ga-beam at 5 kV to remove regions potentially severely damaged by the implantation of energetic Ga ions. The specimen was then analysed by APT in a Cameca LEAP 5000 XR (**Table S1**) fitted with a reflectron-lens with a detector efficiency of ~52%. The specimen was analysed in laser pulsing mode at 50 K with a laser pulse energy of 80 pJ focused on an area estimated to be <3 μm in diameter, a detection rate of 0.5 ion detected for 100 pulses and a laser pulse repetition rate of 125 kHz. The data processing and reconstruction were done with the commercial software package AP Suite 6.1. The compositional profile presented herein was generated from a cylindrical region of interest using the 1D concentration profile function and computed using the fixed bin width profile, atomic, and decompose complex ions options. The bin size was adjusted to 0.05 nm to maximize the ratio of the peak signal to the statistical fluctuations. The ranged mass spectrum used for the specimens is shown in **Figure S2**.

3. Results

EMP X-ray maps of the garnet porphyroclasts reveal compositional variations across the grains (**Figure 3**). Relative to the core, the rims of the porphyroclasts have a Ca-rich and Fe- and Mg-depleted composition, similar to that of the neocrystallized garnet grains (**Figure 3**).

EBSD analysis of the garnet porphyroclasts reveals minor evidence for crystal-plastic deformation within the brittle-dominated grain fragments. Inverse pole figure (IPF) maps of two large (220 × 225 µm; 175 × 195 µm) porphyroclasts reveal a cross-cutting band of smaller grains (1–10 µm in diameter) exhibiting a wide distribution of crystal orientations (**Figure 4a, 5**). The IPFs for the large grains reveal minor dispersion relative to the main orientation (**Figure 5a–c**) whereas small grains show scattered and random orientations, and therefore no obvious systematic misorientation relationship to the orientation of the adjacent larger grains (**Figure 5d–e**). Deviation angle and grain boundary maps reveal lattice distortions within the large grains as heterogeneous misorientation patterns with a maximum misorientation of 36° relative to the grain average (**Figure 4b**), and low-angle grain boundary (LAGB) development at the large grain rims (**Figure 4c**). Within the larger grains, the misorientation angle of the LAGBs gradually increase from 2–5° in the grain interior to 5–15° near the rim (**Figure 4c**). This contrasts with the smaller grains that exhibit almost no evidence for intragranular lattice distortion and are primarily bordered by high-angle grain boundaries (HAGB; **Figure 4b–c**). Note, regularly spaced fractures completely overprint the misorientation patterns within the garnet clasts and do not appear related to crystal-plastic microstructures.

High-contrast BSE imaging also shows the nearly parallel and regularly spaced fractures overprinting the porphyroclasts (**Figure 4d**), yet these fractures do not propagate into the host quartzofeldspathic matrix. Smaller (1–10 µm) subgrains within the larger clasts are apparent as greyscale variations at the rims of the porphyroclasts (**Figure 4d–f**). Small grains within the band display polygonal to slightly lobate grain boundaries (**Figure 4e–f**) with localized microfracturing along the HAGBs (**Figure 3d-f)**. HAGBs display noticeably brighter contrasts, indicative of segregation of a heavier element, confirmed by EDX mapping revealing Fe enrichment and Mg depletion (**Figure 6**).

APT analysis from a HAGB (**Table S1**) reveals a homogeneous distribution of the major garnet components (8.28 at% Mg; 2.16 at% Ca; 11.04 at% Al; 11.30 at% Si, 48.68 at% O), except for Fe (12.87 at%; **Table 1**). Iron is homogenously distributed in region 1, with a composition of 8.40 at%, whereas in region 2 it makes up 18.79 at% of the bulk composition. Moreover, it forms regular planar arrays of near-spherical nanoclusters with diameters of 3.0–7.5 nm and spacing of 2.0–7.5 nm between the clusters. The distance between the planar arrays is 4.5–6.5 nm. The average composition of the clusters, extracted from Fe isosurfaces (isovalue: 0.34), reveals mostly Fe enrichment (49.69 at%) with the other garnet components making up the remaining composition (**Figure 7, Table 1**). The Fe-rich nanoclusters are also highlighted by the distribution of Ga ions within the specimen (**Figure S3**).

4. Discussion

4.1 Deformation mechanisms of garnet

The microstructures documented by EBSD and BSE analyses suggest the garnet porphyroclasts deformed dominantly by brittle to brittle-plastic mechanisms. Plastically deformed regions with the highest degree of misorientation and the development of LAGBs within the garnet are spatially related to the rims of porphyroclasts (**Figure 4**). In the semi-brittle regime of deformation, fracturing can generate dislocations; therefore, fracturing and dislocation glide processes can be superimposed and act reciprocally (Rogowitz et al., 2018; McLaren and Pryer, 2001; FitzGerald et al., 1991). Since plastic deformation in our sample is concentrated at the rims of porphyroclasts, fracturing during cataclasis of the granulite facies porphyroblasts likely played an important role in generating dislocations and facilitating the onset of crystal-plasticity during eclogite facies deformation. Although assumed to be a high-strength mineral in crustal strength profiles (Karato et al., 1995; Wang and Ji, 1999), both brittle and crystal-plastic behaviour have been reported in naturally deformed garnet (e.g., Austrheim et al., 2017; Hawemann et al., 2019a). Experimental deformation studies on garnet conclude that differential stresses on the order of a few gigapascals are required to produce shear fractures in the mineral, and the onset of crystal-plastic deformation for natural strain rates (10^{-12}–10^{-15} s^{-1}; Behr and Platt, 2011) should only occur at temperatures above 640–750°C (Karato et al., 1995; Wang and Ji, 1999). The estimated peak temperature for our sample (~650°C) falls within the range of the proposed transition from brittle to crystal-plastic deformation. Our micro- and nanostructural data are consistent with previous studies evincing brittle and crystal-plastic deformation of garnet under such temperature conditions within mylonitic shear zones related to seismic stresses (Hawemann et al., 2019a).

EBSD IPF maps and plots (**Figure 4a, 5**) reveal a band of 1–10 µm, relatively strain-free grains with scattered orientations. Progressive subgrain rotation due to dislocation glide and creep processes is an effective mechanism to generate new, small grains during dynamic recrystallization at moderate homologous temperatures (Hobbs, 1968). During recrystallization, there is a systematic relationship, termed host-control, between host grains, progressively rotated subgrains, and recrystallized grains (Halfpenny et al. 2006; Stünitz et al., 2003). In our sample, the LAGBs within the larger grains reveal gradually increasing misorientation angles towards the rims. The same systematic relationship can be observed in their respective IPF plots which show minor dispersion around the main grain orientation. However, within the fine-grained band, there is no systematic relationship between the larger (host) grains and the smaller grains. Therefore, subgrain rotation recrystallization alone cannot completely explain the band of small, strain-free grains in our sample.

Instead, we propose that at eclogite facies conditions the small grains were derived from fragments of the host granulite grains due to comminution during cataclastic deformation, and underwent various degrees of rotation. Fragments generated by cataclasis, typically have irregular shapes (Stünitz and FitzGerald, 1993), yet in our sample, these small grains display polygonal to slightly lobate grain boundaries, suggesting that the grain boundaries were mobile. Grain boundary mobility can occur due to either the high surface energy of small grains, which can drive normal grain growth and solid-state recrystallization, or the difference in dislocation density between the neighbouring fractured and non-fractured zones within the grains, leading to dynamic recrystallization by bulging or grain boundary migration (GBM; Stünitz et al., 2003; Tullis and Yund, 1992). Polygonal grain boundaries within the fine-grained band (**Figure 4e, f**) corroborate that normal grain growth occurred during metamorphism. Although GBM could explain the lobate grain boundaries, the low homologous temperature experienced by the sample combined with the lack of crystal-plasticity unrelated to brittle structures, make GBM highly unlikely. If dynamic recrystallization did occur, then it most likely did so by bulging.

Based on these combined observations, we suggest that the small, relatively strain-free grains represent former fragments of the host porphyroclast, which acted as nuclei for grain growth at during the eclogite facies deformation. The nucleation of new grains by cataclasis and subsequent growth of very small fragments leading to the non-host control orientation of recrystallized grains has also been documented in plagioclase and quartz deformed at low homologous temperatures (Hirth and Tullis, 1992; Stünitz et al., 2003).

Moreover, the large set of fractures overprinting the garnet porphyroclasts suggest that the garnet underwent at least two stages of brittle deformation (**Figure 1, 2**). The first being the cataclastic deformation of granulite facies porphyroblasts, which is related to crystal-plasticity indicating it occurred at the peak temperatures. The second stage formed the regularly spaced fractures, which occur nearly perpendicular to the host rock foliation. The lack of crystal-plastic microstructures associated with these fractures, and the presence of retrograde biotite infilling the open space, suggest this stage of brittle deformation occurred after the peak temperatures had dropped below the brittle to crystal-plastic transition for garnet (640–750°C; Karato et al., 1995; Wang and Ji, 1999). The development of regularly spaced opening-mode fractures occurring perpendicular to the garnet layer and terminating at the interface between garnet and the softer quarzofeldspathic host rock is consistent with micro-jointing reported in layered materials (Bai et al., 2000). A study on garnet from the same location in the Musgrave Province has interpreted this second generation of extensional fractures to be related to exhumation of the eclogite facies rocks (Hawemann et al., 2019a).

4.2 Nature and composition of nanoclusters

The Fe-rich composition of the nanoclusters was confirmed by estimating the field-strength conditions during field evaporation through the Kingham analysis method (**Figure S4**; Kingham, 1981). Based on the ratio of Al^{3+} to Al^{2+} (0.08) in the mass spectrum, the field conditions for the nanoclusters can be estimated at 40 Vnm^{-1}. Under such field conditions, and even though the Kingham analysis can only provide an estimate, the field evaporation and post-ionization of Si causes the ions to be detected only in the double charge state, therefore minimizing any overlap at 28 Da and confirming the Fe-rich composition of the nanoclusters.

The Fe-rich nanoclusters are also highlighted by the distribution of Ga ions in the specimen (**Figure S3a**). In the 3D reconstruction, Ga (peak at 69 Da) is concentrated both at the tip of the specimen and along the Fe nanoclusters. No other combination of elements could explain the peak observed at 69 Da apart from the implantation of the monoisotopic Ga used in the FIB preparation. This observation is consistent with previous studies showing that when Ga is mobile in the structure, it tends to segregate along pre-existing defects during FIB-based specimen preparation (Gault et al., 2018). Intentional segregation of Ga has even been used in the past to reveal specific phases inside a specimen, including far from the specimen's topmost surface (Ruan et al. 2011). In addition, the 3D reconstruction of another specimen from the same lift-out also shows Ga enrichment at the specimen surface, but no Fe nanoclusters are observed despite the penetration of the ions (**Figure S3b**). The presence of Ga implantation and the absence of clusters in the second specimen suggests the Fe nanoclusters did not result from ion implantation during specimen preparation. Moreover, the diffusion of Fe in garnet at room temperature is not expected to be fast enough to form such clusters as a result of ion implantation or the associated change in the material's composition (Li et al. 2018). Finally, the accelerated diffusion of Ga on the half where clusters are present could be explained by a combination of ion channeling and the Ga affinity for Fe.

4.3 Origin of nanocluster arrays

EDX mapping of the HAGBs within the fine-grained band shows Fe enrichment and Mg depletion (**Figure 6**), which is confirmed in the APT data revealing Fe enrichment in the form of planar and nearly equally spaced arrays of Fe-rich nanoclusters (**Figure 7**). Although many studies have previously reported elemental differences at LAGBs and HAGBs in garnets (e.g., Chapman et al. 2017, 2019a, 2019b; Konrad-Schmolke et al. 2007; Tacchetto et al. 2022), none have documented nanocluster arrays. Such a regular arrangement of nanoclusters is strikingly similar to those documented in some metallic alloys (e.g., Yen et al., 2011; Seol et al., 2017). In those instances, cooling of the designed alloy transforms it from a high-temperature face-centered cubic phase to a low-temperature body-centred cubic phase. The phase transformation leads to nanoparticles continuously nucleating and subsequently detaching from the migrating heterophase interface, resulting in regular planar arrays of nanoparticles within the bulk material. The thermal treatment of the metal allows for precise control of the dispersion of these property-enhancing precipitates, and hence of the alloy’s beneficial mechanical properties (e.g., yield strength, high-temperature strength, and creep resistance; Ashby, 1958; Devaraj et al., 2016; Orowan, 1968; Vogel et al., 2013). When densely arranged in the metallic matrix, these nanoparticles indeed act as effective obstacles for dislocation movement apportioning only small volumes for dislocations to move freely. Known as the Orowan effect, dislocations must either loop around or sweep through the nanoparticles to accommodate strain, requiring relatively higher amounts of energy and therefore stresses (Ashby, 1958; Orowan, 1968).

We propose that a very similar nanostructuring has occurred in the garnet at a mobile grain boundary. The mobility of the HAGBs within the fine-grained band is driven by normal growth and solid-state recrystallization during metamorphism (**Figure 8a**), as illustrated by the EBSD data. Grain boundaries in crystalline materials have a high transport coefficient for diffusing atoms and are the loci of solute segregation driven by the reduction in the system's free energy (Raabe et al., 2014). Therefore, we suggest that Fe was segregated into the core of grain boundaries during growth, leading to solute drag (**Figure 8b**; e.g., Luo et al., 2022), which slows down the grain boundary, further facilitating high degrees of segregation. Upon reaching a critical Fe-concentration at the grain boundary, phase separation occurred and Fe-rich nanoclusters nucleated on the grain boundary, similar to localized spinodal decomposition (Kwiatkowski et al., 2018). The continuous migration of the grain boundaries during growth leaves behind planar alignments of equally sized and spaced nanoclusters (**Figure 8c**), forming regular planar arrays in the vicinity of HAGBs (**Figure 8d**). Although the precipitates that form within doped alloys segregate due to the inability of the trace elements to reside within the transformed phase, Fe is a major component of garnet and should be stable within the crystal structure. EPMA X-ray maps of the garnet porphyroclasts reveal Ca-enriched rims that are depleted in Fe and Mg (**Figure 3**). Camacho et al. (2009) studied these same rocks and interpreted the chemical variations as a result of Ca diffusion from the enriched host-rock into the garnet rims. The diffusion of Ca therefore reduced the solubility of Fe and Mg in the crystal structure, leading to their diffusion out of the garnet. Therefore, the uptake of Ca and the reduced solubility of Fe within the growing garnet grains can explain the segregation of Fe into nanoclusters rather than its homogeneous distribution.

These regular arrays of Fe-rich nanoclusters in the garnet may have acted as barriers for migrating dislocations. This process can lead to hardening, dislocation tangles, and facilitates intragranular mechanical failure of the garnet prophyroclast through microfracture nucleation at and propagation along grain boundaries (**Figure 8e, f**). The propagation of fractures along grain boundaries can in turn promote the localization of crystal-plasticity creating a positive feedback loop. The microfractures observed at HAGBs (**Figure 4e**) in conjunction with Fe-segregation (**Figure 4b**) in our sample are consistent with this model.

Conclusion

We have combined 2D and 3D structural and chemical analyses on garnet porphyroclasts from the relatively dry lower crust of the Musgrave Province (central Australia) to identify the micro- and nanoscale processes associated with deformation in the brittle- to brittle-plastic regime of garnet. EBSD and EDX data reveal a band of randomly oriented small grains outlined by Fe-rich HAGBs formed by cataclasis and subsequent growth. APT data from one of these HAGBs reveals regular planar arrays of Fe-rich nanoclusters. The combined data led us to propose a new strain hardening model in garnet whereby the mobility of grain boundaries during growth led to the formation of regular planar arrays of Fe-rich nanoclusters that act as barriers for migrating dislocations. The arrest of the dislocations resulted in defect tangles and microfracture nucleation and propagation at grain boundaries. Localized hardening in garnet in the vicinity of grain boundaries, as documented herein, can therefore potentially contribute to the mechanisms of mechanical failure within the presumed high-strength mineral. The occurrence of strain-hardening in garnet potentially contributes to crustal strengthening in the lower crust, which could lead to deep seismicity.

Acknowledgement

RD was funded by an NSERC Postdoctoral Fellowship. RD and BG are grateful for funding from the DFG through the Leibniz Prize 2020. Andreas Sturm, Uwe Tezins and the APT group at MPIE are thanked for their training and support. We greatly appreciate discussions with Xuyang Zhou (MPIE, Düsseldorf), Stefan Zaefferer (MPIE, Düsseldorf) and Luca Menegon (UiO, Oslo). Comments on an earlier version of this manuscript from Luiz Morales (ETH, Zurich) and two anonymous reviewers helped clarify our message.

References

Ashby, M., 1958, Oxide Dispersion Strengthening, *in* Ansell, G. et al., eds, Gordon and Breach, New York, p. 143.

Audet, P., and Bürgmann, R., 2011, Dominant role of tectonic inheritance in supercontinent cycles: Nature Geoscience, v. 4, p. 184–187, doi: 10.1038/ngeo1080

Austrheim, H., and Boundy, T., 1994, Pseudotachylytes generated during seismic faulting and eclogitization of the deep crust: Science, v. 265, p. 82–83, doi: 10.1126/science.265.5168.82

Austrheim, H., Dunkel, K., Plümper, O., Ildefonse, B., Liu, Y., and Jamtveit, B., 2017, Fragmentation of wall rock garnets during deep crustal earthquakes: Science Advances, v. 3, p. 1–7, doi: 10.1126/sciadv.1602067

Bai, T., Pollard, D.D., and Gao, H., 2000, Spacing of edge fractures in layered materials: International Journal of Fracture, v. 103, p. 373–395, doi: 10.1023/A:1007659406011

Behr, W., and Platt, J., 2011, A naturally constrained stress profile through the middle crust in an extensional terrane: Earth and Planetary Science Letters, v. 303, p. 181–192, doi: 10.1016/j.epsl.2010.11.044

Bürgmann, R., Dresen, G., 2008, Rheology of the lower crust and upper mantle: evidence from rock mechanics, geodesy, and field observations: Annual Reviews in Earth and Planetary Sciences, v. 36, p. 531–567, doi: 10.1146/annurev.earth.36.031207.124326

Burov, E.B., and Watts, A.B., 2006, The long-term strength of continental lithosphere: "jelly sandwich" or "crème brûlée"?, GSA Today, v. 16, p. 4–10, doi: 10.1130/1052 5173(2006)016<4:TLTSOC>2.0.CO;2

Byerlee, J., 1978, Friction of Rocks, *in*: Byerlee, J.D., Wyss, M., eds, Rock Friction and Earthquake Prediction, Contributions to Current Research in Geophysics (CCRG), v. 6. Birkhäuser, Basel, doi: 10.1007/978-3-0348-7182-2_4

Camacho, A., and Fanning, C., 1995, Some isotopic constraints on the evolution of the granulite and upper amphibolite facies terranes in the eastern Musgrave Block, central Australia: Precambrian Research, v. 71, p. 155–181, doi: 10.1016/0301-9268(94)00060-5

Camacho, A., Compston, W., McCulloch, M., and McDougall, I., 1997, Timing and exhumation of eclogite facies shear zones, Musgrave Block, central Australia: Journal of Metamorphic Geology, v. 15, p. 735–751, doi: 10.1111/j.1525-1314.1997.00053.x

Camacho, A., Yang, P., and Frederiksen, A., 2009, Constraints from diffusion profiles on the duration of high-strain deformation in thickened crust: Geology, v. 37, p. 755–758, doi: 10.1130/G25753A.1

Chapman, T., Clarke, G.L., Piazolo, S., and Daczko, N.R., 2017, Evaluating the importance of metamorphism in the foundering of continental crust: Scientific Reports, v. 7, 13039, doi: 10.1038/s41598-017-13221-6

Chapman, T., Clarke, G.L., Piazolo, S., and Daczko, N.R., 2019b, Inefficient high-temperature metamorphism in orthogneiss: American Mineralogist, v. 104, p. 17–30, doi: 10.2138/am-2019-6503

Chapman, T., Clarke, G.L., Piazolo, S., Robbins, V.A., and Trimby, P.W., 2019a, Grain-scale dependency of metamorphic reaction on crystal plastic strain: Journal of Metamorphic Geology, v. 37, p. 1021–1036, doi: 10.1111/jmg.12473

Collerson, K.D., Oliver, R.L., and Rutland, R.W.R., 1972, An example of structural and metamorphic relationships in the Musgrave orogenic belt, central Australia: Journal of the Geological Society of Australia, v. 18, p. 379–393, doi: 10.1080/00167617208728776

Devaraj, A., Joshi, V.V., Srivastava, A., Manandhar, S., Moxson, V., and Duz, V.A., 2016, A low-cost hierarchical nanostructured beta-titanium alloy with high strength: Nature Communications, v. 7, 11176, doi: 10.1038/ncomms11176

Ellis, D.J., and Maboko, M.A.H., 1992, Precambrian tectonics and physicochemical evolution of the continental crust: I—The gabbro-eclogite transition: Precambrian Research, v. 55, p. 491–506, doi: 10.1016/0301-9268(92)90041-L

Ellis, S., and Wang, K., 2022, Lithospheric strength and stress revisited: Pruning the Christmas tree: Earth and Planetary Science Letters, v. 595, 117771, doi: 10.1016/j.epsl.2022.117771

FitzGerald, J., Boland, J., McLaren, A., Ord, A., and Hobbs, B., 1991, Microstructures in water-weakened single crystals of quartz: Journal of Geophysical Research, v. 96B, p. 2139–2155, doi: 10.1029/90JB02190

Gault, B., Breen, A.J., Chang, Y., He, J., Jägle, E.A., Kontis, P., Kürnsteiner, P., Kwiatkrowski da Silva, A., Makineni, S.K., Mouton, I., Peng, Z., Ponge, D., Schwarz, T., Stephenson, L.T., Szczepaniak, A., Zhao, H., and Raabe, D., 2018, Interfaces and defect composition at the near-atomic scale through atom probe tomography investigations: Journal of Materials Research, v. 33, p. 4018–4030, doi: 10.1557/jmr.2018.375

Giuntoli, F., Lanari, P., and Engi, M., 2018, Deeply subducted continental fragments – Part 1: Fracturing, dissolution–precipitation, and diffusion processes recorded by garnet textures of the central Sesia Zone (western Italian Alps): Solid Earth, v. 9, p. 167–189, doi: 10.5194/se-9-167-2018

Goetze, C., and Evans, B., 1979, Stress and temperature in the bending lithosphere as constrained by experimental rock mechanics: Geophysical Journal International, v. 59, p. 463–478, doi: 10.1111/j.1365-246X.1979.tb02567.x

Gray, C., 1978, Geochronology of granulite – facies gneisses in the western Musgrave Block, Central Australia: Journal of the Geological Society of Australia, v. 25, p. 403–414, doi: 10.1080/00167617808729050

Green, H., and Houston, H., 1995, The mechanics of deep earthquakes: Annual Review of Earth and Planetary Sciences, v. 23, p. 169–213, doi: 10.1146/annurev.ea.23.050195.001125

Hacker, B., Peacock, S., Abers, G., and Holloway, S., 2003, Subduction factory 2. Are intermediate-depth earthquakes in subducting slabs linked to metamorphic dehydration reactions?: Journal of Geophysical Research: Solid Earth, v. 108, no. 2030, p. 1–16, doi: 10.1029/2001JB001129

Halfpenny, A., Prior, D.J., and Wheeler, J., 2006, Analysis of dynamic recrystallization and nucleation in a quartzite mylonite: Tectonophysics, v. 427, p. 3–14, doi: 10.1016/j.tecto.2006.05.016

Hawemann, F., Mancktelow, N.S., Wex, S., Camacho, A., and Pennacchioni, G., 2018, Pseudotachylyte as field evidence for lower-crustal earthquakes during the intracontinental Petermann Orogeny (Musgrave Block, Central Australia): Solid Earth, v. 9, p. 629–648, doi: 10.5194/se-9-629-2018

Hawemann, F., Mancktelow, N., Wex, S., Pennacchioni, G., and Camacho, A., 2019a, Fracturing and crystal plastic behaviour of garnet under seismic stress in the dry lower continental crust (Musgrave Ranges, Central Australia): Solid Earth, v. 10, p. 1635–1649, doi: 10.5194/se-10-1635-2019

Hawemann, F., Mancktelow, N.S., Pennacchioni, G., Wex, S., and Camacho, A., 2019b, Weak and slow, strong and fast: How shear zones evolve in a dry continental crust (Musgrave Ranges, Central Australia): Journal of Geophysical Research-Solid Earth, v. 124, p. 219–240, doi: 10.1029/2018JB016559

Hirth, G., and Tullis, J., 1992, Dislocation creep regimes in quartz aggregates: Journal of Structural Geology, v. 14, p. 145–159, doi: 10.1016/0191-8141(92)90053-Y

Hobbs, B., 1968, Recrystallization of single crystals of quartz: Tectonophysics, v. 6, p. 353–401, doi: 10.1016/0040-1951(68)90056-5

Ingrin, J., and Madon, M., 1995, TEM observations of several spinel-garnet assemblies: Toward the rheology of the transition zone: Terra Nova, v. 7, p. 509–515, doi: 10.1111/j.1365-3121.1995.tb00552.x

Jackson, J., 2002, Faulting, flow, and the strength of the continental lithosphere. International Geology Review, v. 44, p. 39–61, doi: 10.2747/0020-6814.44.1.39

Ji, S. C., Saruwatari, K., Mainprice, D., Wirth, R., Xu, Z, and Xia, B., 2003, Microstructures, petrofabrics and seismic properties of ultra high-pressure eclogites from Sulu region, China: Implications for rheology of subducted continental crust and origin of mantle reflections: Tectonophysics, v. 370(1– 4), p. 49– 76, doi: 10.1016/S0040-1951(03)00177-X

Jin, Z.M., Zhang, J., Green, H.W., and Jin, S., 2001, Eclogite rheology: Implications for subducted lithosphere: Geology, v. 29, p. 667–670, doi: 10.1130/0091-7613(2001)029<0667:ERIFSL>2.0.CO;2

Karato, S., Wang, Z., Liu, B., and Fujino, K., 1995, Plastic deformation of garnets: systematics and implications for the rheology of the mantle transition zone: Earth and Planetary Science Letters, v. 130, p. 13–30, doi: 10.1016/0012-821X(94)00255-W

Kavner, A., 2007, Garnet yield strength at high pressures and implications for upper mantle and transition zone rheology: Journal of Geophysical Research, v. 112, B12207, doi: 10.1029/2007JB004931

Kingham, D.R., 1982, The post-ionization of field evaporated ions: A theoretical explanation of multiple charge states: Surface Science, v. 116, p. 273–301, doi: 10.1016/0039-6028(82)90434-4

Kirkpatrick, J., and Rowe, C., 2013, Disappearing ink: How pseudotachylytes are lost from the rock record: Journal of Structural Geology, v. 52, p. 183–198, doi: 10.1016/j.jsg.2013.03.003

Kohlstedt, D.L., Evans, B., and Mackwell, S.J., 1995, Strength of the lithosphere: constraints imposed by laboratory experiments: Journal of Geophysical Research, v. 100, p. 17587–17602, doi: 10.1029/95JB01460

Konrad-Schmolke, M., O'Brien, P.J., and Heidelbach, F., 2007, Compositional re-equilibration of garnet: The importance of sub-grain boundaries: European Journal of Mineralogy, v. 19, p. 431–438, doi:10.1127/0935-1221/2007/0019-1749.

Kwiatkowski da Silva, A., Ponge, D., Peng, Z., Inden, G., Lu, Y., Breen, A., Gault, B., and Raabe, D., 2018, Phase nucleation through confined spinodal fluctuations at crystal defects evidenced in Fe-Mn alloys: Nature Communications, v. 9, p. 1–11, doi: 10.1038/s41467-018-03591-4

Li, B., Ge, J., and Zhang, B., 2018, Diffusion in garnet: a review: Acta Geochimica, v. 37, p. 19–31, doi: 10.1007/s11631-017-0187-x

Luo, T., Mangelinck, D., Serrano-Sánchez, F., Fu, C., Felser, C., and Gault, B., 2022, Grain boundary in NbCo(Pt)Sn half-Heusler compounds: Segregation and solute drag on grain boundary migration: Acta Materialia, v. 226, p. 1–9, doi: 10.1016/j.actamat.2021.117604

Mainprice, D., Bascou, J., Cordier, P., and Tommasi, A., 2004, Crystal preferred orientations of garnet: comparison between numerical simulations and electron back-scattered diffraction (EBSD) measurements in naturally deformed eclogites: Journal of Structural Geology, v. 26, p. 2089–2102, doi: 10.1016/j.jsg.2004.04.008

Major, R.B., 1973, Explanatory Notes for the Woodroffe 1 V 250000 Geological Map SG/52-12, 1st Edn., Adelaide, Australia, Geological Survey of South Australia.

Mancktelow, N., Camacho, A., and Pennacchioni, G., 2022, Time-lapse record of an earthquake in the dry felsic lower continental crust preserved in a pseudotachylyte-bearing fault: Journal of Geophysical Research: Solid Earth, v. 127, p. 1–32, doi: 10.1029/2021JB022878

McLaren, A., and Pryer, L., 2001, Microstructural investigation of the interaction and interdependence of cataclastic and plastic mechanisms in feldspar crystals deformed in the semi-brittle field: Tectonophysics, v. 335, p. 1 –15, doi: 10.1016/S0040-1951(01)00042-7

Orowan, E., 1968, Precipitation Hardening, 1st ed., *in* Martin, J., ed., Pergamon Press, Oxford, p. 201–202.

Papa, S., Pennacchioni, G., Angel, R.J., and Faccenda, M., 2018, The fate of garnet during (deep-seated) coseismic frictional heating: The role of thermal shock: Geology, v. 46, p. 471–474, doi: 10.1130/G40077.1

Phillips, N.J., and Ji, S., 2021, Constraining the ductile deformation mechanisms of garnet across pressure-temperature space: Journal of Structural Geology, v. 148, 104356, doi: 10.1016/j.jsg.2021.104356

Raabe, D., Herbig, M., Sandlöbes, S., Li, Y., Tytko, D., Kuzmina, M., Ponge, D., and Choi, P.-P., 2014, Grain boundary segregation engineering in metallic alloys: A pathway to the design of interfaces: Current Opinion in Solid State & Materials Science, v. 18, p. 253–261, doi: 10.1016/j.cossms.2014.06.002

Rempel, A., and Rice, J., 2006, Thermal pressurization and onset of melting in fault zones: Journal of Geophysical Research, v. 111, B09314, doi: 10.1029/2006JB004314

Rogowitz, A., Zaefferer, S., and Dubosq, R., 2018, Direct observation of dislocation nucleation in pyrite using combined electron channeling contrast imaging and electron backscatter diffraction: Terra Nova, v. 30, p. 423–430, doi: 10.1111/ter.12358

Ruan, H., Torres, K.L., Thompson, G.B., and Schuh, C.A., 2011, Gallium-enhanced phase contrast in atom probe tomography of nanocrystalline and amorphous Al–Mn alloys: Ultramicroscopy, v. 111, p. 1062–1072, doi: 10.1016/j.ultramic.2011.01.026

Seol, J., Na, S.-H., Gault, B., Kim, J.-E., Han, J.-C., Park, C.-G., and Raabe, D., 2017, Core-shell nanoparticle arrays double the strength of steel: Scientific Reports, v. 7, p. 1–9, doi: 10.1038/srep42547

Stünitz, H., and FitzGerald, J., 1993, Deformation of granitoids at low metamorphic grade, II: Granular flow in albite-rich mylonites: Tectonophysics, v. 221, p. 299–324, doi: 10.1016/0040-1951(93)90164-F

Stünitz, H., FitzGerald, J., and Tullis, J., 2003, Dislocation generation, slip systems, and dynamic recrystallization in experimentally deformed plagioclase single crystals: Tectonophysics, v. 372, p. 215–233, doi: 10.1016/S0040-1951(03)00241-5

Tacchetto, T., Reddy, S.M., Fougerouse, D., Clark, C., Saxey, D.W., and Rickard, W.D.A., 2022, Crystal plasticity enhances trace element mobility in garnet: Geology, doi: 10.1130/G50283.1

Thompson, K., Lawrence, D., Larson, D., Olson, J., Kelly, T., and Gorman, B., 2007, In situ site-specific specimen preparation for atom probe tomography: Ultramicroscopy, v. 107, p. 131–139, doi: 10.1016/J.ULTRA MIC.2006.06.008

Trepmann, C.A, and Stöckhert, B., 2002, Cataclastic deformation of garnet: a record of synseismic loading and postseismic creep: Journal of Structural Geology, v. 24, p. 1845–1856.

Tullis, J., and Yund, R., 1992, Chapter 4: the brittle-ductile transition in feldspar aggregates: an experimental study, *in* Evans, B., and Wong, T.-F., eds, International Geophysics, Academic Press, p. 89–117, doi: 10.1016/S0074-6142(08)62816-8

Villaseca, C., Downes, H., Pin, C., and Barbero, L., 1999, Nature and Composition of the Lower Continental Crust in Central Spain and the Granulite–Granite Linkage: Inferences from Granulitic Xenoliths: Journal of Petrology, v. 40, p. 1465–1496, doi: 10.1093/petroj/40.10.1465

Vogel, F., Wanderka, N., Balogh, Z., Ibrahim, M., Stender, P., Schmitz, G., and Banhart, J., 2013. Mapping the evolution of hierarchical microstructures in a Ni-based superalloy: Nature Communications, v. 4, 2955, doi: 10.1038/ncomms395512

Wang, K., 2021, If not brittle: ductile, plastic, or viscous?: Seismological Research Letters, v. 92, p. 1181–1184, doi: 10.1785/0220200242

Wang, Z., and Ji, S., 1999, Deformation of silicate garnets; brittle-ductile transition and its geological implications: Canadian Mineralogist, v. 37, p. 525–541.

Wex, S., Mancktelow, N.S., Camacho, A., and Pennacchioni, G., 2019, Interplay between seismic fracture and aseismic creep in the Woodroffe Thrust, central Australia – Inferences for the rheology of relatively dry continental mid-crustal levels: Tectonophysics, v. 758, p. 55–72, doi: 10.1016/j.tecto.2018.10.024

White, J.C., 2012, Paradoxical pseudotachylyte – Fault melt outside the seismogenic zone: Journal of Structural Geology, v. 38, p. 11–20, doi: 10.1016/j.jsg.2011.11.016

Yen, H., Chen, P., Huang, C., Yang, J., 2011, Interphase precipitation of nanometer-sized carbides in a titanium–molybdenum-bearing low-carbon steel: Acta Materialia, v. 59, p. 6264–6274, doi: 10.1016/j.actamat.2011.06.037

Table 1. Bulk composition analysis of garnet specimen

	Whole specimen			Region 1			Region 2			Clusters isosurfaces		
Ion Type	**Count**	**Atomic %**	**σ**	**Count**	**Atomic %**	**σ**	**Count**	**Atomic %**	**σ**	**Count**	**Atomic %**	**σ**
H	104727	5.24	0.06	53861	4.94	0.10	50299	5.49	0.07	3485	2.64	0.13
O	972809	48.68	0.13	575857	52.84	0.24	404072	44.07	0.15	47299	35.85	0.38
Si	225859	11.30	0.09	136093	12.49	0.17	88695	9.67	0.11	2698	2.04	0.21
Ca	43189	2.16	0.03	23826	2.19	0.06	19148	2.09	0.04	1536	1.16	0.08
Mg	165546	8.28	0.07	95885	8.80	0.13	68594	7.48	0.07	4867	3.69	0.13
Al	220509	11.04	0.08	109755	10.07	0.14	108385	11.82	0.09	6581	4.99	0.16
Mn	7910	0.40	0.02	2669	0.24	0.04	5243	0.57	0.03	0	0.00	0.00
Fe	257151	12.87	0.09	91576	8.40	0.15	172258	18.79	0.12	65558	49.69	0.40
In	390	0.02	0.00	290	0.03	0.01	91	0.01	0.01	0	0.00	0.00
Cr	174	0.01	0.00	67	0.01	0.01	99	0.01	0.00	3	0.00	0.01
Total	1998264	100		1089879	100		916884	100.00		132027	100	

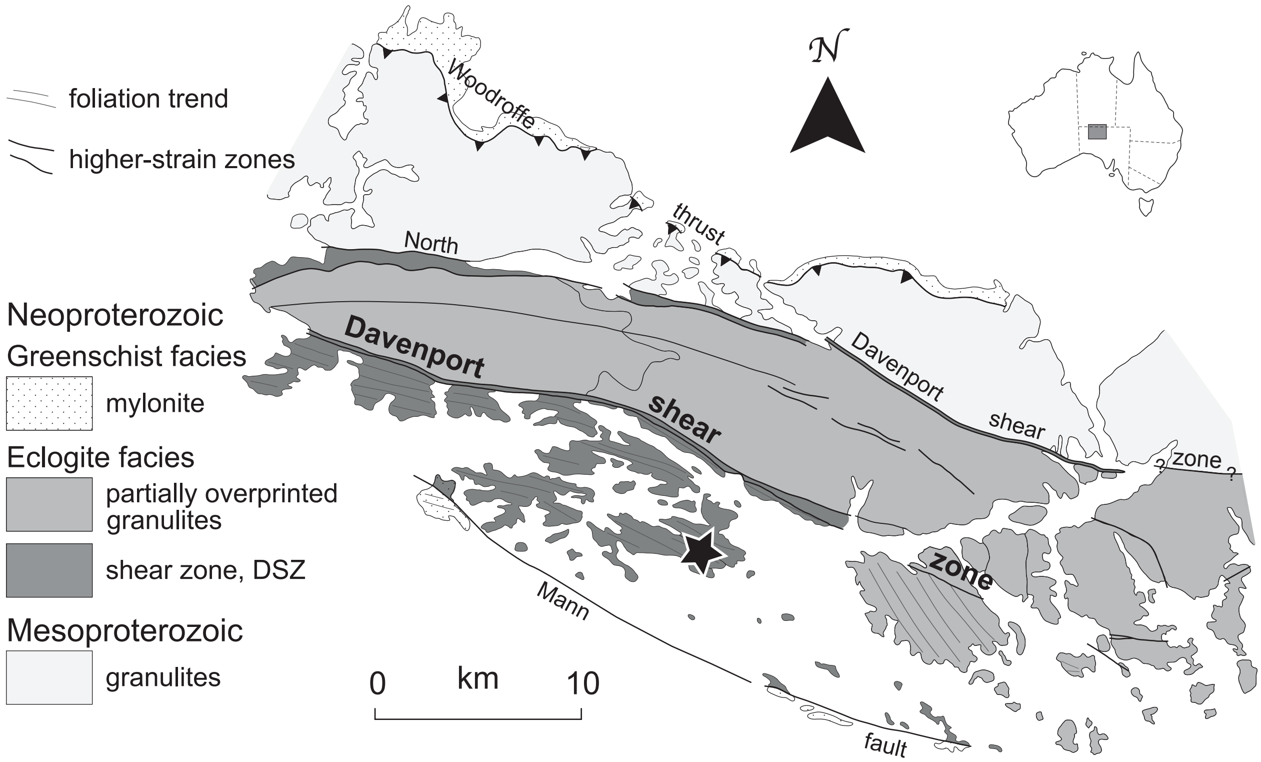

Figure 1. Simplified geological map of Mount Woodroffe region, South Australia, showing the sample location (black star; S26° 24.386' E131° 39.171' Datum WGS84) between the Davenport shear zone (DSZ) and the Mann fault. Modified after Camacho et al. (2009).

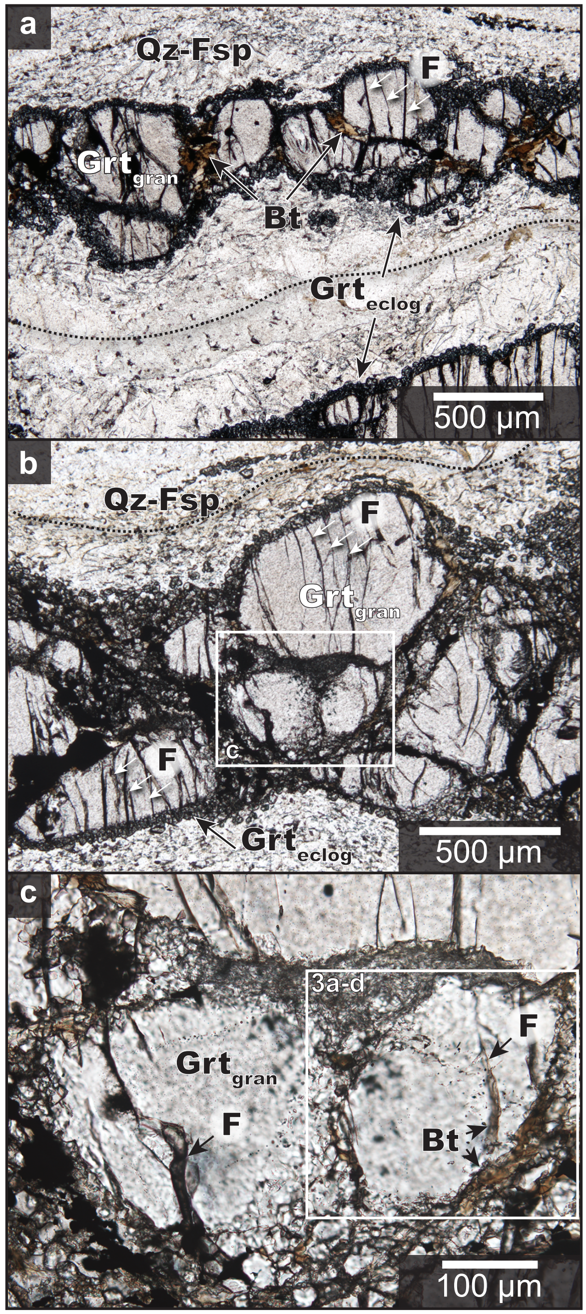

Figure 2. a-c Photomicrographs (PPL) of the investigated garnet porphyroclasts hosted within a mylonitic Qz-Fsp matrix, Musgrave Province, central Australia. Granulite facies garnet porphyroclasts (Grtgran) form foliation parallel bands and are overgrown by small neocrystallized eclogite facies garnet porphyroblasts (Grteclog). Both generations of garnet are overprinted by regularly-spaced and foliation perpendicular fractures (F). Foliation is indicated by the dashed black lines. Biotite occurs between garnet porphyroclasts and fractures. White box in b shows the location of image c. White box in c shows the location of Figure 3a-d.

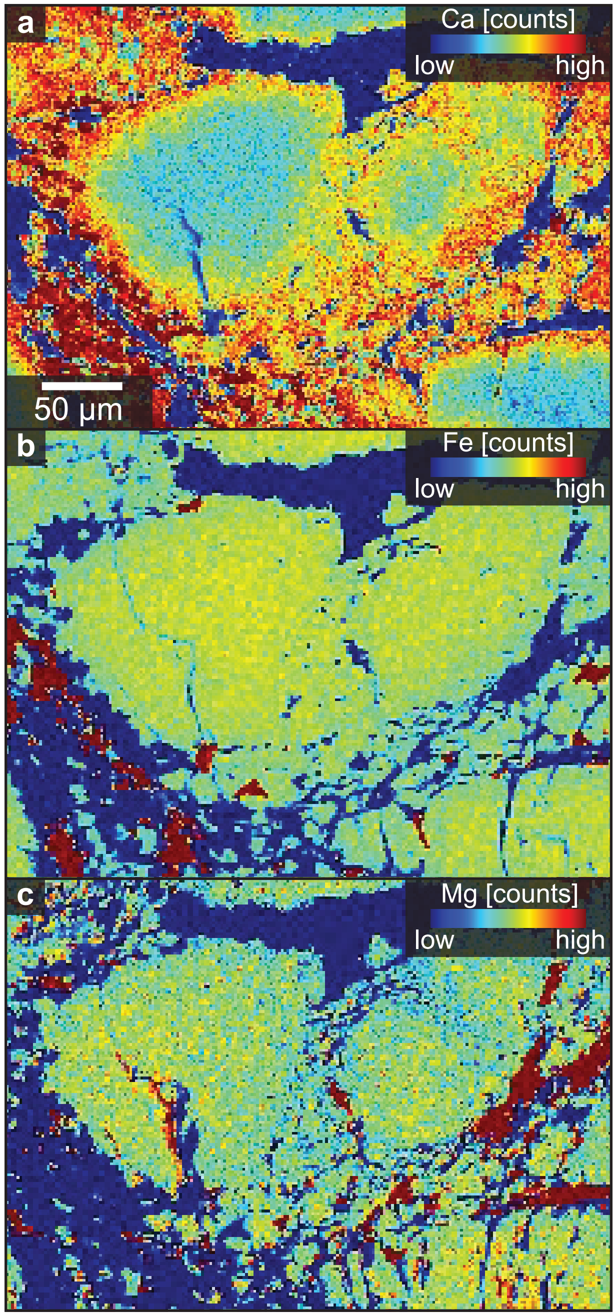

Figure 3. EPM X-ray map for Ca (**a**), Fe (**b**) and Mg (**c**) showing compositional variations along the rims the garnet prophyroclasts shown in Figure 2c. Clast rims are enriched in Ca and depleted in Fe and Mg relative to cores.

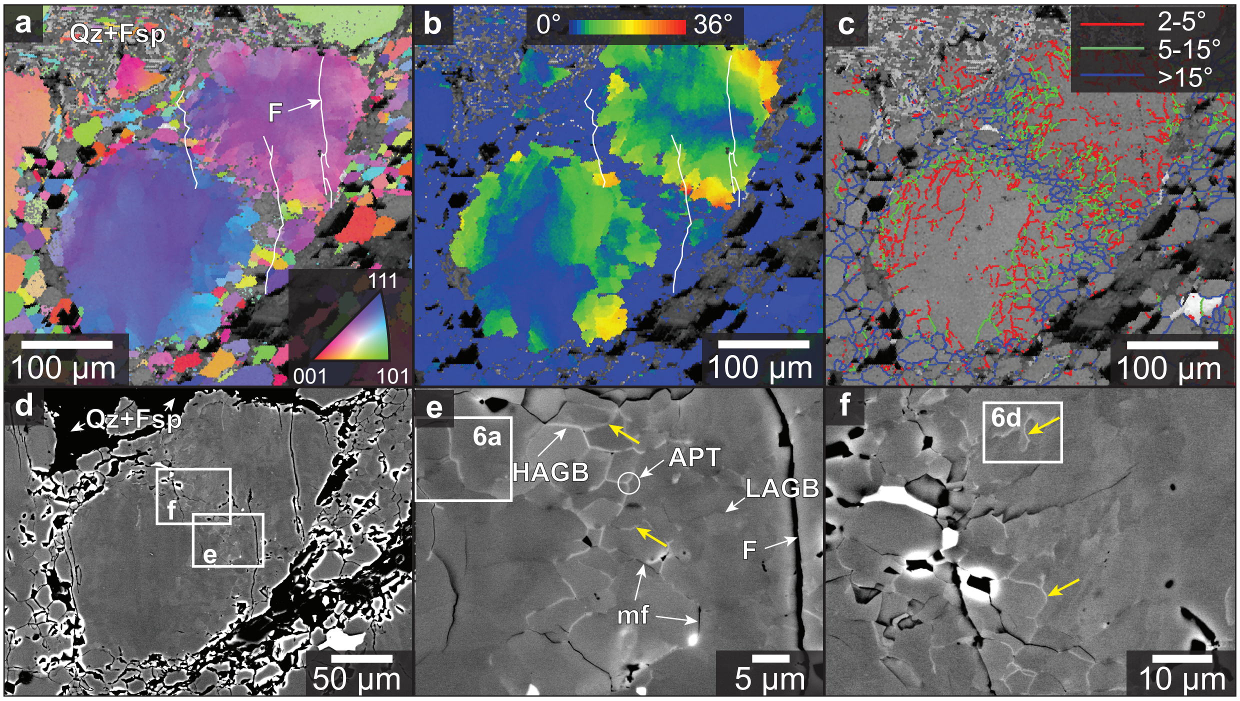

Figure 4. a IPF map of garnet porphyroclasts showing the band of smaller grains with scattered orientations between two larger grains. Fractures from BSE image are traced in white (F). **b** Orientation deviation angle map revealing a heterogeneous misorientation pattern within the larger grains with higher misorientation along the rims (max. misorientation of 36°) and relatively no misorientation within the smaller grains. **c** Grain boundary map evincing the development of LAGBs with increasing misorientation angle towards the rims of the large grains and HAGBs within the fine-grained band. **d-f** High-contrast BSE images revealing LAGBs within the larger grains and HAGBs within the band of smaller grains. Small grains within the band exhibit polygonal to slightly lobate grain boundaries (yellow arrows). Note: microfracturing (mf) along HAGBs. Images (e) and (f) show the location of the APT specimen (e) and the EDX maps (e, f).

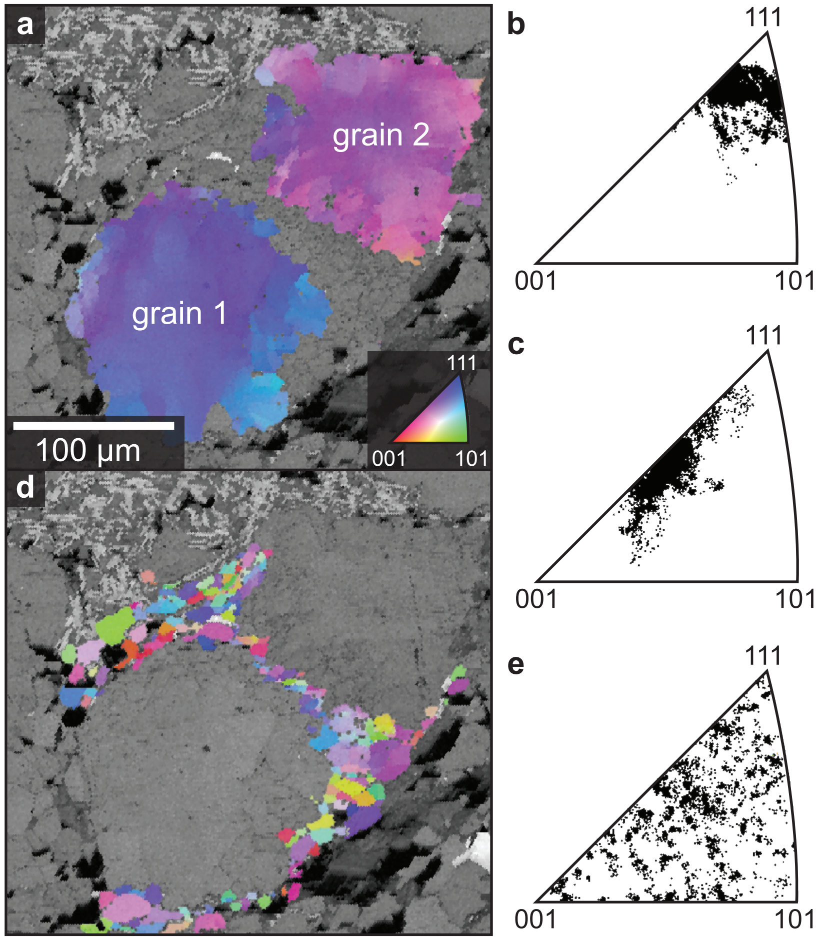

Figure 5. a IPF map of larger grains 1 and 2. **b–c** Lower hemisphere IPF plots of grains 1 (c) and 2 (d) showing minor dispersion relative to the main orientation of the grains. **d** IPF map of fine-grained band. **e** Lower hemisphere IPF plot of the fine-grained band showing the large distribution of orientations within the smaller grains with no relationship to the larger grains' orientations.

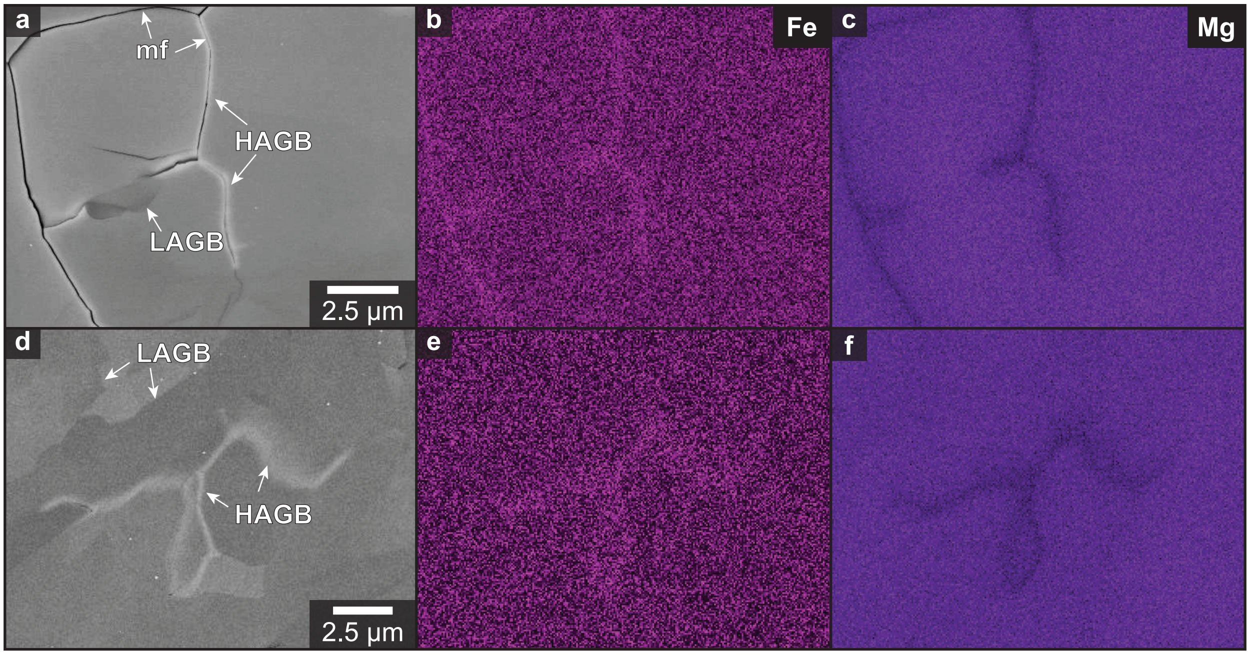

Figure 6. BSE images (**a, d**) and EDX maps of Fe (**b, e**) and Mg (**c, f**) within the garnet porphyroclast revealing Fe enrichment and Mg depletion at fractured (mf) and intact HAGBs.

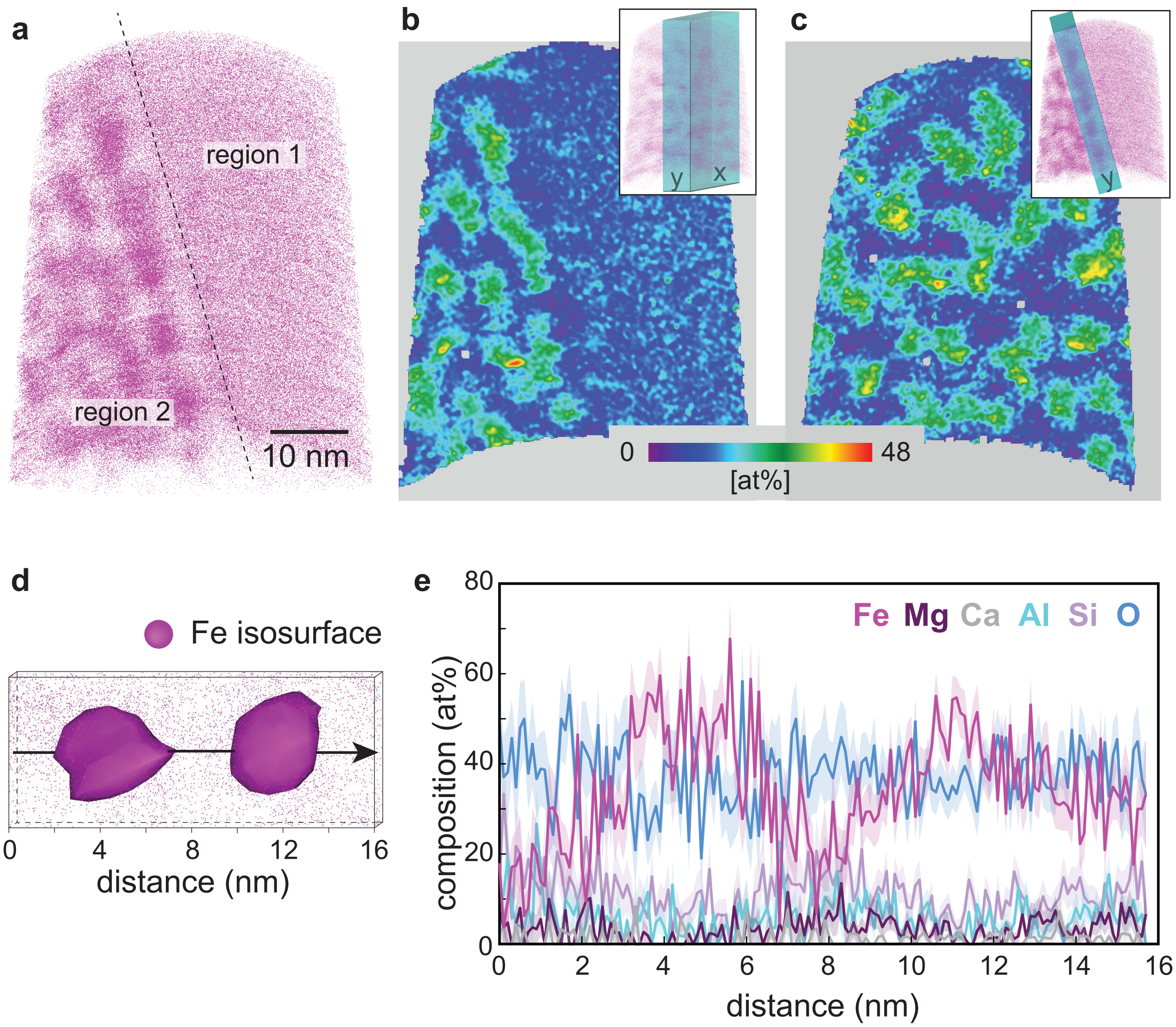

Figure 7. **a** 3D reconstruction of APT specimen revealing Fe-rich nanoclusters aligned into individual planes on the left side of the specimen (region 2). Note: Fe peaks at 28 and 56 Da are plotted in the figure. Details on ranging the peak at 28 Da can be found in Figure S2. **b** and **c** 2D contour plot showing the projection of Fe compositions along the y-axis of a region of interest perpendicular (b) and parallel (c) to the Fe-nanocluster planes. The regions of interest for (b) and (c) are shown as turquoise boxes in the inset APT reconstructions on the upper right corner of each image. **d** Clipping of region of interest surrounding two Fe-rich nanoclusters (pink isosurfaces; 34 at% isovalue). **e** Composition profile across the two clusters in (d) confirming Fe enrichment (54.7–67.7 at%) and slightly depleted Si, Mg, Al, and O compositions within the matrix between clusters.

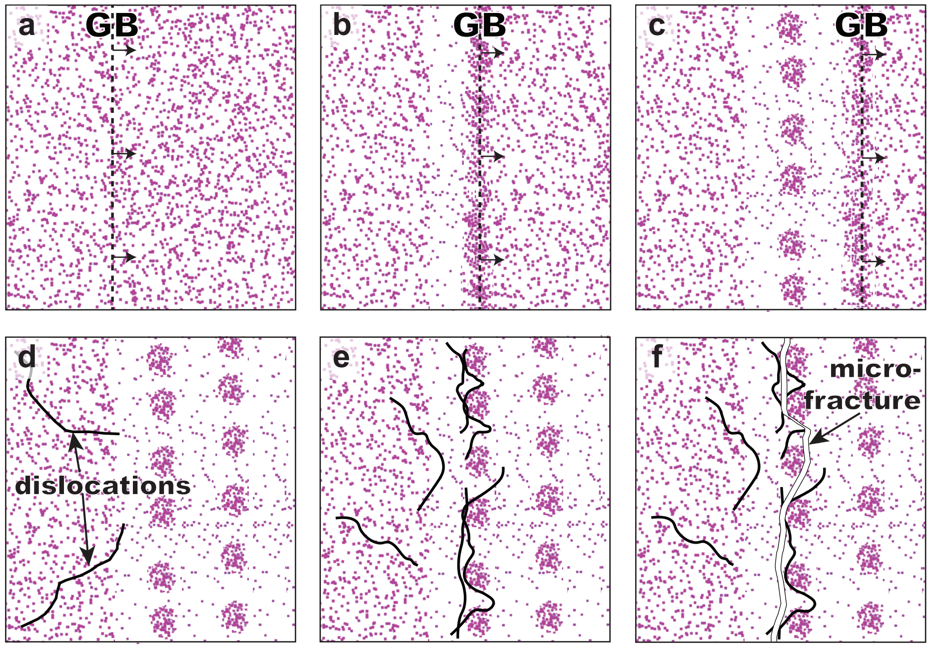

Figure 8. Conceptual model of strain hardening in garnet. **a** Initial state of grain boundary (GB) prior to migration during crystal growth. **b** Accumulation of Fe within the core of the migrating grain boundary leaving behind an Fe-depleted wake. **c** Nucleation and detachment of Fe nanoclusters after reaching saturation and continued crystal growth. **d** Introduction and migration of dislocations (thick black lines) during deformation. **e** Continued migration of dislocations and pinning at Fe nanoclusters, leading to entanglement. **f** Nucleation of microfracture at dislocation tangles.

Table S1. Atom probe tomography data acquisition settings and data summary

Specimen/Data set	Specimen i
Instrument Model	LEAP 5000 XR
Instrument settings	
Laser wavelength (nm)	355
Laser pulse energy (pJ)	80
Voltage pulse fraction (%)	n.a.
Pulse frequency (kHz)	125
Evaporation control	detection rate
Target detection rate (ions/pulse)	0.005
Nominal flight path (mm)	382
Set point temperature (K)	50
Chamber pressure (Torr)	4.66E-11
Data summary	
LAS root version	18.46.533c
CAMECAROOT version	18.46.533c
Analysis software	AP Suite 6.1
Total ions:	3070985
Single (%)	63.7
Multiple (%)	34.8
Partial (%)	1.5
Reconstructed ions:	2371612
Ranged (%)	87.5
Unranged (%)	12.5
Volt./bowl corr. peak (Da)	32
Mass calib. (peaks/interp.)	5/Lin.
$(M/\Delta M)$ for ^{28}Fe	933.3
$(M/\Delta M_{10})$	50.9
Time-independent background (ppm/ns)	24
Reconstruction	
Final specimen state	fractured
Pre-/post-analysis imaging	SEM/n.a
Radius evolution model	voltage
Field factor (k)	3.3
Image compression factor	1.65
Assumed E-field (V/nm)	25
Detector efficiency (%)	52
Avg. atomic volume (nm^3)	species specific volume used (see range file)
Vinitial; Vfinal (V)	3140; 4125

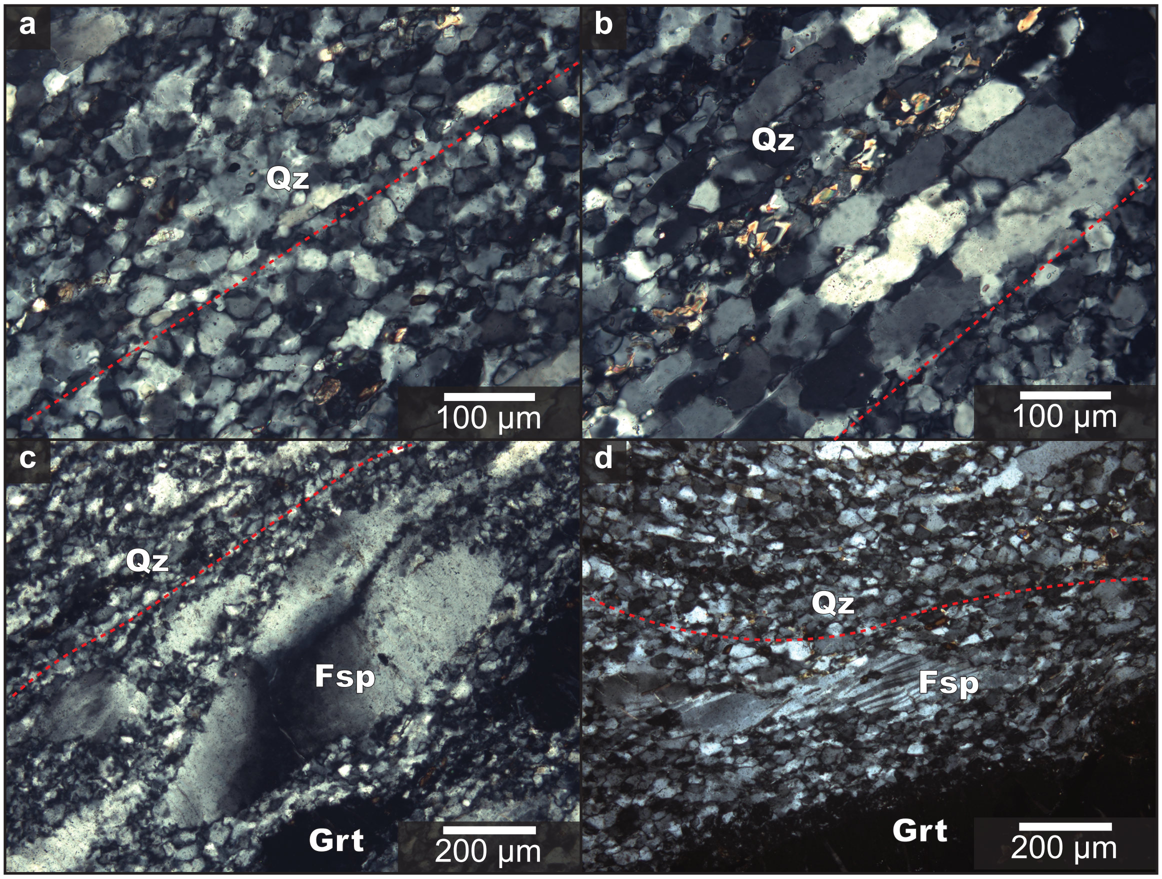

Figure S1. a-d Photomicrographs (XPL) of deformed quartzofeldpathic mylonite matrix. Main foliation is traced by dashed red lines. a Fine-grained (<50 μm) quartz with serrated grain boundaries and slightly larger elongated grains (up to 100 200 μm) exhibiting undulose extinction, deformation bands, and new subgrains forming around the edges. b foliation parallel quartz ribbons (30 100 μm) with undulose extinction and polygonal subgrain development. c-d medium to coarse grained (0.2–0.5 mm 0.5–2.5 mm) elongated lenticular porphyroclasts oriented parallel to the main foliation with undulose extinction, folded and tapered twinning, and new subgrain development around the edges.

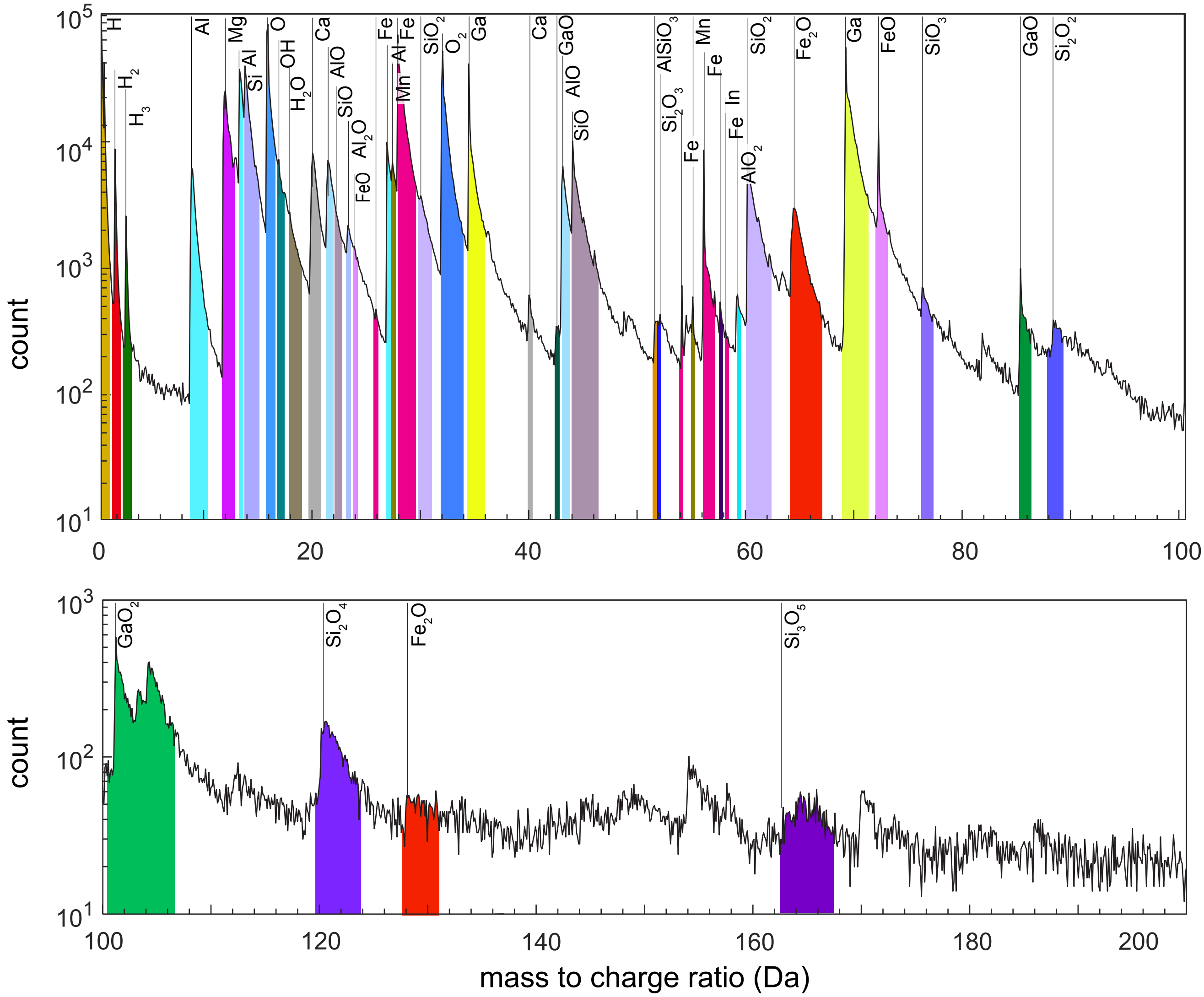

Figure S2. Atom probe mass spectrum of garnet specimen

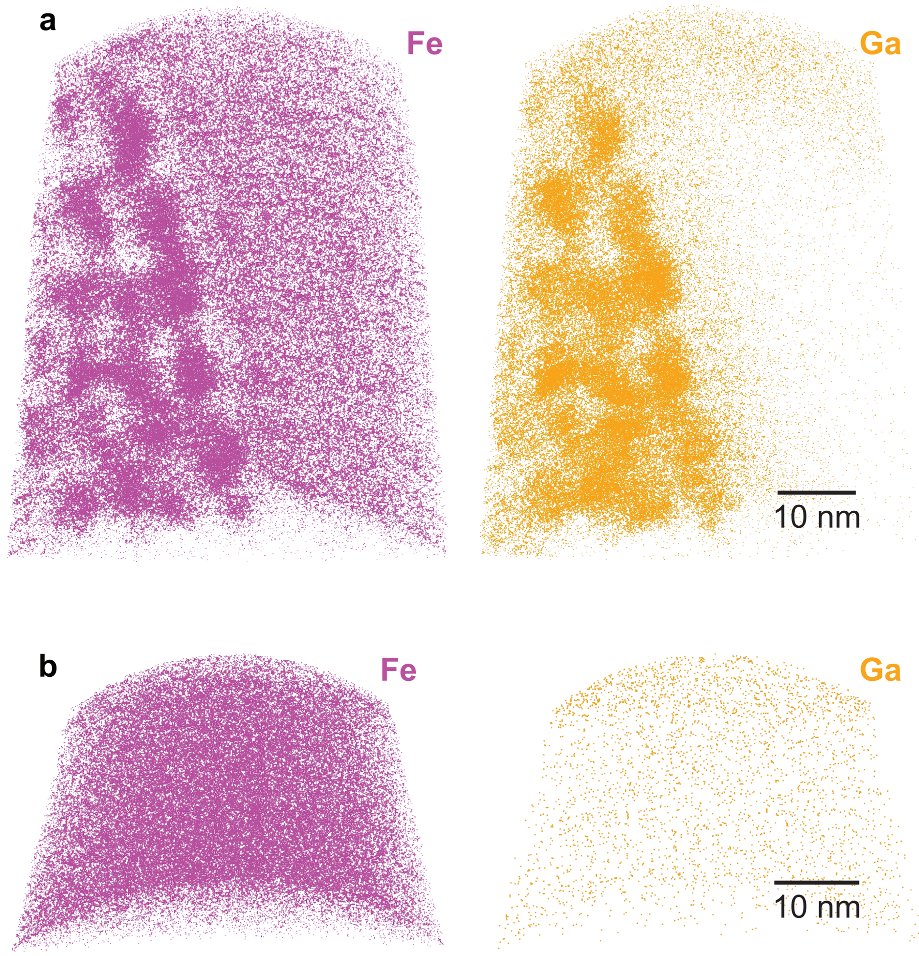

Figure S3. a 3D reconstruction of the investigated APT specimen showing the distribution of Fe and Ga. Note: Ga is concentrated both at the tip of the specimen and the within the Fe nanoclusters. **b** 3D reconstruction of another APT specimen from the same lift-out showing the distribution of Fe and Ga. Note: Ga is also enriched at specimen the surface, but no Fe nanoclusters are observed despite the penetration of the ions. The presence of Ga implantation and the absence of clusters in the second specimen (b) suggests the Fe nanoclusters did not result from ion implantation during specimen preparation.

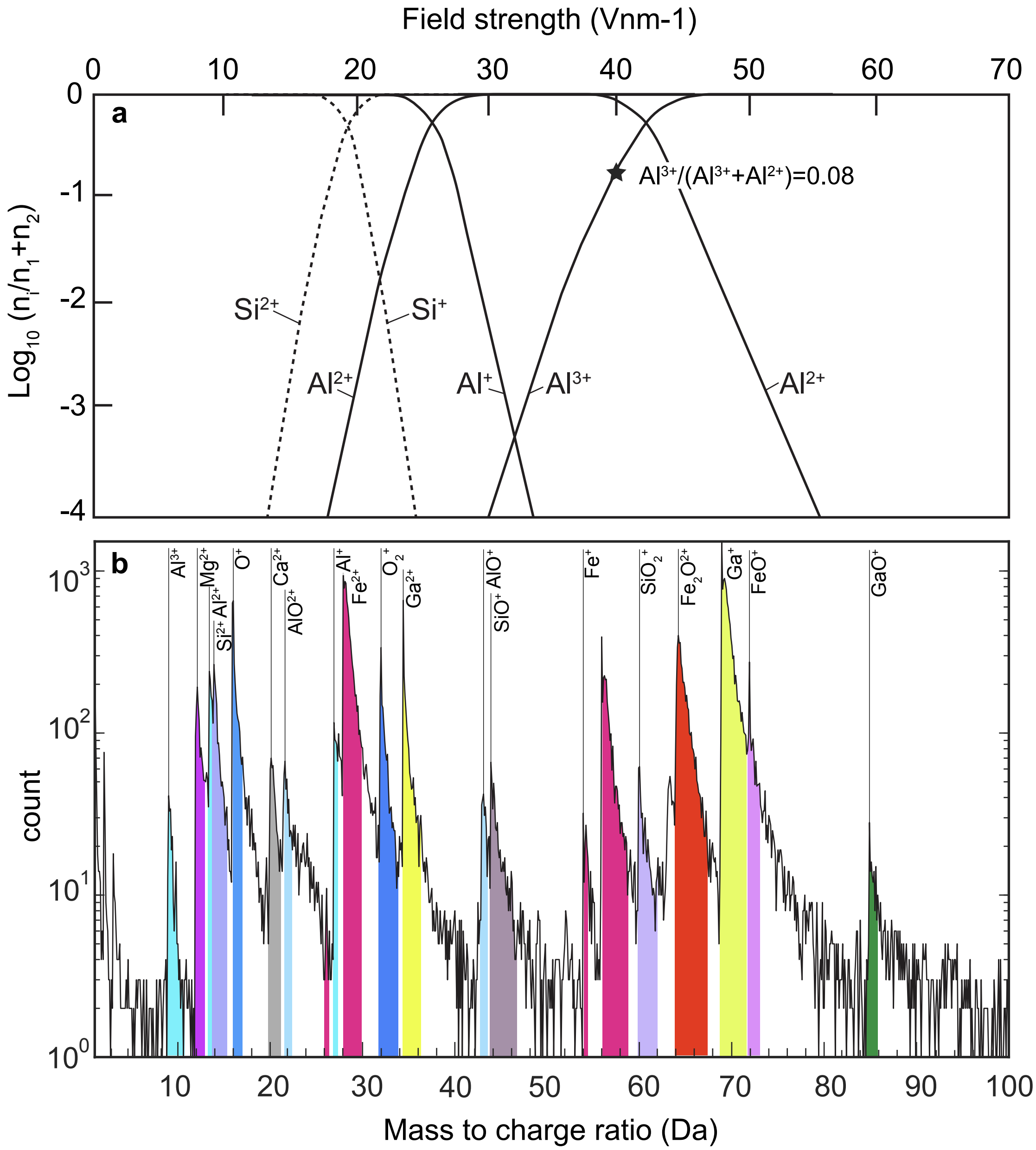

Figure S4. a Relative abundance of different charge states for Al and Si during field evaporation plotted logarithmically against field strength (modified after Kingham, 1981). **b** Mass spectrum of Fe nanoclusters extracted from isosurfaces (34 at% isovalue). The ratio of Al3+ to Al2+ (0.08) in the mass spectrum estimates the field conditions for the clusters at 40 Vnm-1, where Si is expected to field evaporate and post-ionise to be detected only in the double charge state.